In Situ Observation of the Atomic-scale High-temperature Phase Transition Enhancement Mechanism at the ODS-W Interface

Guoqing Wei
Hefei University of Technology
Luo Laima (luolaima@126.com)
Hefei University of Technology
Qi Zhang
Hefei University of Technology
Xuepeng Liu
Hefei University of Technology
Yifan Zhang
Hefei University of Technology
Haixin Li
Beijing University of Technology Science park
Zhipeng Li
Beijing University of Technology
Yu-Cheng Wu
Hefei University of Technology

Article

Keywords:

Posted Date: April 28th, 2022

DOI: https://doi.org/10.21203/rs.3.rs-1574521/v1

In Situ Observation of the Atomic-scale High-temperature Phase Transition Enhancement Mechanism at the ODS-W Interface

Guoqing Wei,[1] Laima Luo,[145*] Qi Zhang,[2] Xuepeng Liu,[2] Yifan Zhang,[14] Haixin Li,[3] Zhipeng Li,[6] Yucheng Wu[145*]

[1] *School of Materials Science and Engineering, Hefei University of Technology, Hefei 230009, China*

[2] *Institute of Industry & Equipment Technology, Anhui Province Key Lab of Aerospace Structural Parts Forming Technology and Equipment, Hefei University of Technology, Hefei 230009, China*

[3] *Beijing University of Technology Science park, Building 29, Yard 1, Jinghai Fifth Road, Tongzhou District, Beijing 100176, China*

[4] *Engineering Research Center of High Performance Copper Alloy Materials and Processing, Ministry of Education, Hefei 230009, China*

[5] *National-Local Joint Engineering Research Centre of Nonferrous Metals and Processing Technology, Hefei 230009, China*

[6] *Beijing Key Laboratory of Microstructure and Property of Advanced Materials, Beijing University of Technology, Beijing 100124, China.*

Correspondence should be addressed to the authors: luolaima@126.com; ycwu@hfut.edu.cn.

Rare earth oxide doping Metal is a common strengthening method for metal matrices. Recent studies show that the ODS-W alloys exhibit a more superior mechanical properties at higher temperatures, but the underlying strengthening mechanism is obscure due to the experimental technical limitations. This study performed in situ tensile deformations at temperatures up to 1273 K inside a transmission electron microscope with atomic-scale resolution. The results uncovered that the crack source caused by tension is at the W grain boundary, rather than the expected weak interface between W and oxide. We showed that the W near the ODS-W interface occurs BCC–FCC phase transition and breaks away from the W matrix. By combining molecular dynamics simulation with first-principle theory calculations, we confirmed that the W_{FCC} matrix after the BCC–FCC phase transition possesses excellent adhesion work, which remarkably enhances the W and the oxide bonding force. Based on these observations, we proposed a high-temperature phase transformation strengthening method, which provides essential guidance for oxide-strengthen alloys at high temperatures and adds new ideas to the second-phase strengthening mechanism.

The strengthening mechanisms of metal materials can roughly divided into two types. One is to increase the alloying atoms' interatomic bonding force to increase their academic strength to obtain a perfect crystal without defects. The other is to introduce flaws in the crystal, such as dislocations, point defects, heterogeneous atoms, grain boundaries, and highly dispersed particles or heterogeneous structures (e.g., segregation). The movement of dislocations is hindered by these defects, which results in a significant improvement in strength. The main strengthening methods include solid solution strengthening[1-3], second-phase particle strengthening[4,5], fine grain strengthening[6-8], and work hardening[9-11]. As a standard strengthening method, the second-phase particle strengthening is widely used in structural materials like tungsten and molybdenum. For tungsten, the doping of the second phase can improve its mechanical properties and ductile-brittle transition temperature. Because the oxide particles have a high melting point and stable physical and chemical properties, they usually doped in the W matrix as the second phase; ODS-W usually alloy has good mechanical properties, thermal shock resistance, and radiation damage resistance[12-14]. Therefore, doping nano-oxide particles in the W matrix is the primary strengthening means of W as a nuclear fusion-oriented plasmonic material.

Explanations for the strengthening mechanism of ODS alloys are twofold. One is that the second-phase particles inhibit the growth of W matrix grains during the sintering process, and they refine the grain size to achieve the effect of fine-grain strengthening for improving the toughness of pure W[15-16]. The other is that the pinning

effect of uniformly dispersed nanoparticles on dislocation slip and GB migration significantly enhances the strength at high temperature and thermal stability of W alloy[17]. Given that oxide particles are mostly located at grain boundaries, the increase in heterogeneous phases often acts as a source of cracks. Thus, many researchers currently attempt to dissolve particles completely in the crystal, the W–X alloy that is dissolved in the crystal improves the toughness of pure W at room temperature; however, the ODS alloy exhibits an excellent tensile strength at high temperatures[18], and the author could not clearly explain this phenomenon; the superb performance at high temperatures is believed to be due to fine grain strengthening. Owing to the exponential increase of the tensile strength of ODS alloy at high temperatures, the strengthening mechanism of ODS alloy should include fine-grain strengthening and traditional second-phase strengthening, and other strengthening methods.

The microscopic mechanism of metal materials under stress becomes more apparent with the development of electron microscopy techniques, such as the behavior of phase transitions under pressure. The phase transition under the stress of body-centered cubic (BCC) structure metals has been observed by TEM and in situ TEM, such as Nb[19], Mo[20], and Ta[21]. W with the BCC structure is stable at room temperature. The DAC experiment has determined that the W material will not induce a room-temperature phase change even if the stress of up to 423 GPa is applied to it [22]. Some interesting phenomena can be produced in small-size W nanowires, such as twins and inverse twins[23-25], but they cannot meet the phase change conditions and form a new phase. Compared with the phase transition behavior of other BCC structural metals at room temperature, W

exhibits a strong temperature dependence. The phase transition process near the crack tip under high-temperature tensile conditions is captured and reported by in situ TEM[26], and the corresponding molecular dynamics (MD) simulations also confirmed that a phase transition occurs in W at high temperature[27]. Therefore, we predicted that the ODS-W alloy has a phase transition under high-temperature tensile stress, and this phase transition effect increases the tensile strength of the alloy. To observe the microscopic process of ODS-W alloy tensile fracture, A high-temperature real-time mechanical testing and a field emission high-resolution transmission electron microscopy (HRTEM) detection were applied to observe the microscopic process of ODS-W alloy tensile fracture.

This study successfully conducted high-temperature in situ tensile experiments on ODS alloys. Advanced technology from Beijing Bestron Science and Technology and Beijing University of Technology was used[28], which allows in situ stretch deformation at up to 1273 K in a transmission electron microscope with atomic resolution. Using this unique technology, we found for the first time that the oxide particles at the grain boundary interacted with the W matrix at high temperatures, and the W matrix was torn off at the oxide grain boundary; the phase transition of the W matrix induced by the oxide interface under high-temperature tensile conditions was also revealed. Using MD combined with first-principle calculations, we concluded that the W matrix of the FCC phase has a more robust interface binding ability than the W matrix of the BCC phase. In combination with the action mechanism of the second phase observed in situ during high-temperature deformation of the matrix, the high-temperature phase transformation

strengthening theory of the ODS-W matrix was proposed. Finally, the reason for the improved strength and toughness of the alloy at high temperatures was explained.

Results

In situ ODS-W TEM sample preparation and high-temperature tensile characterization system: Nano-oxide dispersion strengthened W–Y_2O_3 alloy with uniform second-phase particles was successfully prepared by wet chemical combined with spark plasma sintering (SPS). Figs. 1(a–c) shows the process of preparing samples through the focused ion beam (FIB) technology. FIB was first used to extract rectangular block material from W–Y_2O_3 block through the FIB milling method, and then the sample was loaded onto the heating chip. Using Pt nanocomposite, the rectangular sample was welded to the tensile beam by ion beam-induced deposition, clearly showing dense W matrix particles and dispersed Y_2O_3 particles, as shown in Fig. 1(b). The ion beam of 30 kV and 80 pA (Fischione Model 1040) was used to reduce the width of the sample from 2 μm to 100 nm. The 30 kV and 1.1 pA ion beam was used to mill the sample into a dog-bone shape. The width of the final stretched sample is 700 nm, and the sample contains two Y_2O_3 particles, as shown in Fig. 1(c). The stretching process is shown in Fig. 1(d). Applying pressure on both sides of the beam causes the sample to be subjected to indirect load and deform, and the temperature loading accuracy controlled by voltage reaches ±0.1 K ; at a heating rate of 20 K/min, the sample can be stably heated to 1273 K[29]. Fig. 1(e)shows the schematic of a high-resolution transmission electron microscope for high-temperature in situ analysis[26].

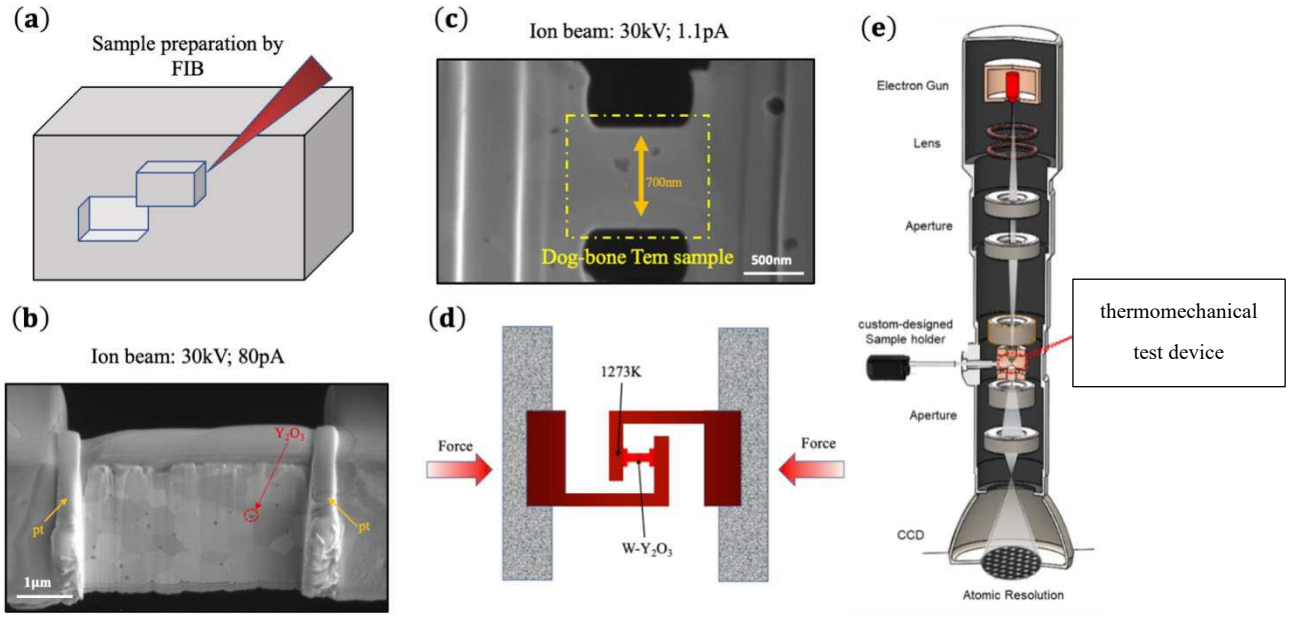

Fig. 1. Preparation and characterization system of in situ W–Y_2O_3TEM sample (a) FIB sample preparation diagram, (b) sample section after welding, (c) shaped in situ W–Y_2O_3TEM tensile sample, (d) working principle diagram of in situ high-temperature stretch rod, (e) high-resolution transmission electron microscope for high-temperature in situ analysis

In situ TEM observation on ODS-W sample of tensile deformation: Fig. 2 shows the in situ TEM observation of W–Y_2O_3 sample of tensile deformation. Fig. 2(a) shows the TEM image of a dog bone-shaped sample installed on a high-temperature mechanical test device. The measurement section size of the sample is 700 nm×600 nm×100 nm, and the sample contains two Y_2O_3 particles, which are located at the grain boundary and the three-fork grain boundary, respectively, as shown in Fig. 2(b). The red particles are Y_2O_3, which are marked as Y_1 and Y_2. Gray line indicates W crystal boundary, and W matrices in the three areas are marked as W_1, W_2, and W_3. At a heating rate of 20 K/min, the sample was first heated to 1273 K and then kept for 10 min to ensure uniform and stable overall temperature. The inset of Fig. 2(a) shows the electron

diffraction (SAED) pattern of selected area of the sample. The selected area is W_1, which is the focus of our subsequent analysis. Figs. 2(c–k) show the sample images at different stages of stretching deformation. A stable tensile force was applied to the sample continuously such that the tensile stress actually acts on the sample, as shown in Fig. 2(c). When the boundary between W_1 and W_2 shows stress concentration area, it is considered a possible source of cracks and defined as 0 s. As the tensile stress increases, the dislocation density continues to increase, and the stress on the crack source gradually increases, as shown in Figs. 2(d–e). At 5 s, the sample cracks along the grain boundary of W_1 and W_3, and the local stress relaxes immediately, as shown in Fig. 2(f). In Fig. 2(g), the yellow dotted circle marks the obvious malposition at the two grain boundaries after the fracture. Then, tension was applied. Figs. 2(h–j) show the sample image after 11, 54, and 73 s of stretching, and the crack gradually expands and slowly extends to Y_2. We will follow up on the in situ TEM analysis of the fracture process at high magnification at Y_2. The sample was further stretched to complete fracture. Fig. 2(k) is the final fracture morphology of the sample, which shows that the sample fractures along the W_1 grain boundary through Y_1 and Y_2. The in situ stretching process reveals no fracture source on the interface of Y_2O_3 and W matrix. The stress concentration at the grain boundary of the W matrix causes fracture, which finally passes through two Y_2O_3 particles along the grain boundary.

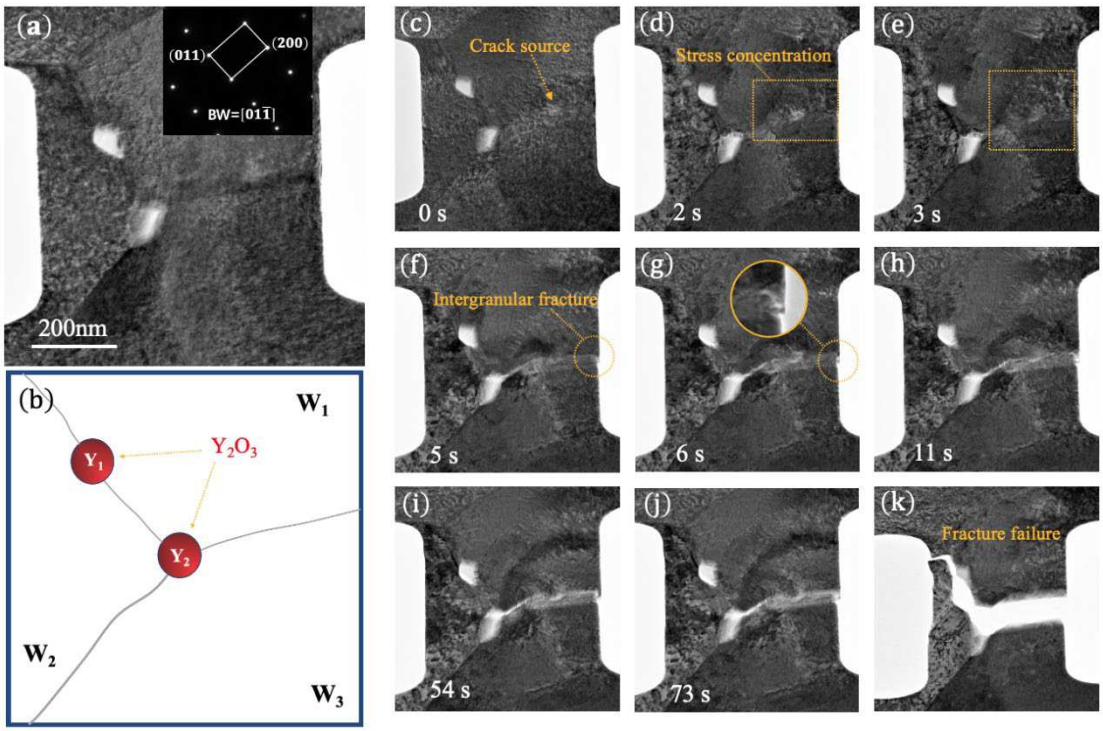

Fig. 2. In situ TEM observation of W–Y_2O_3 sample of tensile deformation (a) TEM image of dog bone-shaped W–Y_2O_3 sample made by FIB, (b) schematic of W–Y_2O_3 sample, (c–i) continuous TEM image at different stages of tensile deformation of the sample at 1273 K , (k) final fracture morphology of W–Y_2O_3 sample

TEM observation of oxide interface after the fracturing of ODS-W sample: Fig. 3 shows the TEM image of the Y_2O_3 interface after fracturing of W–Y_2O_3 sample. Given that the crack source is not at the interface between W matrix and Y_2O_3, a specific abnormal phenomenon is observed at the two interfaces, leading to the enhancement in the binding force of the heterogeneous interface. As shown in Fig. 3(a), two Y_2O_3(Y_1, Y_2) particles were analyzed by HRTEM when the sample was fractured. As observed, the W matrix at the interface of Y_1 and Y_2 is torn. A few W matrices are torn at Y_1(Fig. 3b), and they hang like a drop of water on the interface of Y_1. Multiple drop-like W particles are also found on the surface of Y_2 (Fig. 3c). HRTEM analysis was conducted

for the torn W at Y_1 (Fig. 3d). Fast Fourier transform (FFT) was performed on W in the white box, and the resulting image is e_1. Considering that the torn W is relatively small (5 nm) and the corresponding diffraction spot has only one point, the obtained d^*=4.16 nm^{-1} (Fig. e3), and the d^* value does not match the BCC structure W(JCPDS#04-0806) but matches perfectly with the FCC structure W[30]. The inverse FFT corresponding to the diffraction spot is shown in Fig. e2, where the bright area encircled by a yellow dotted line corresponds to the location of torn W in the white box of Fig. 3(d). This point is indeed the diffraction spots corresponding to torn down W. Thus, the substance on the Y_1 interface is not Y_2O_3 or BCC structure W, but it is most likely the FCC structure W. Similarly, HRTEM analysis was conducted at the Y_2 interface. Two areas with torn W matrices were selected, as shown in Fig. 3(f), and FFT was performed on the white box (Fig. 3g). Given that the Y_2O_3 area is large, the diffraction spot is prominent, and the crystal ribbon axis corresponding to the white parallelogram is $[00\bar{4}]$. The two-crystal plane is the orientation relationship of (200) $(0\bar{2}0)Y_2O_3$(JCPDS#43-0661). The inverse Fourier of the diffraction spot penetrated by the red line is shown in Fig. $3h_1$, where the bright area enclosed by the red dotted line corresponds to the red dotted frame position in Fig. 3(f). It proves that the diffraction spot corresponds to the W matrix torn down in the upper half, and d^*=4.18 nm^{-1} (Fig. $3h_2$). Similarly, the diffraction spot penetrated by the green line corresponds to the W matrix torn down in the lower half, and d^*=4.19 nm^{-1} (Fig. $3l_2$). The two W matrices at Y_2 interface do not match the BCC structure W but fit perfectly with the FCC structure W, and the d^* value corresponds to the $(11\bar{1})$ surface of FCC structure W in Fig. 4.

Combining the HRTEM analysis results of W torn at Y_1–Y_2 interface shows that W leaving the matrix presents an FCC phase. This result is discovered for the first time.

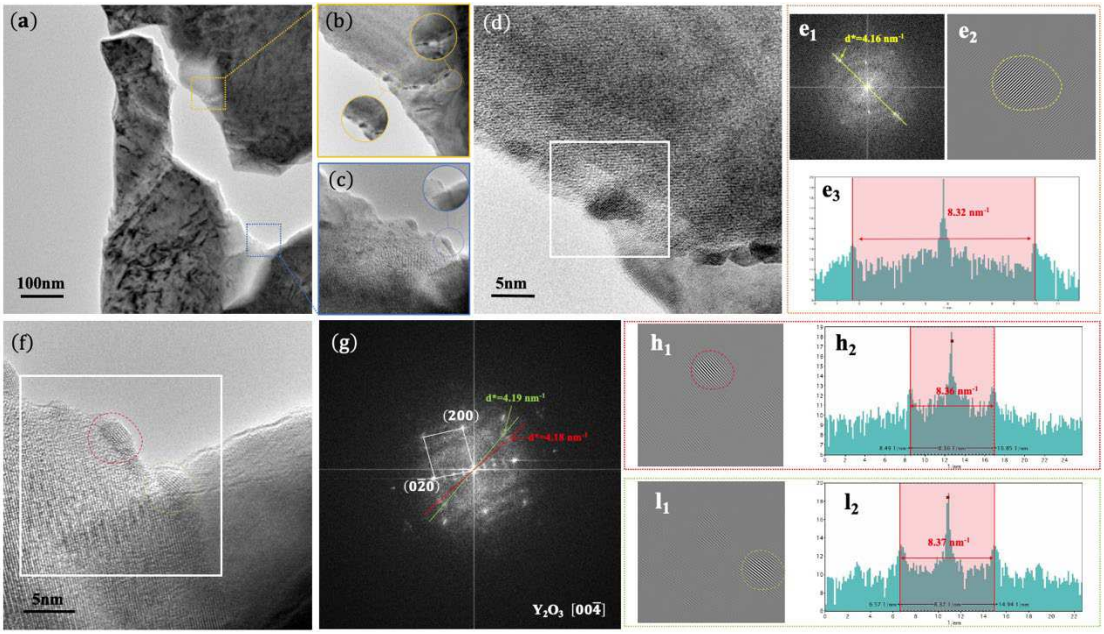

Fig. 3. TEM observation at Y_2O_3 interface after fracture of W–Y_2O_3 sample (a) TEM image of W–Y_2O_3 sample after fracture, (b–c) TEM and partially enlarged view of Y_1–Y_2 interface, (d) HRTEM of Y_1 interface, (e_1–e_3) d^* value of the FFT, inverse Fourier transform, and diffraction spots in the white box of Fig. d, (f) HRTEM of Y_2 interface, (g) FFT in the white box of Fig. f, (h_1–h_2) Inverse Fourier transform corresponding to the red diffraction spot and d^*value in Fig. g, (l_1–l_2) Inverse Fourier transform corresponding to the green diffraction spot and d^* value in Fig. g

BCC–FCC phase transition near the interface of oxide interface and W matrices under tensile load at 1273 K: Fig. 4 shows the TEM image with atomic resolution. Fig. 4(a) is the overall topography of Y_2 after a fracture. Y_2 and the matrix fracture process are shown in the supplementary video 1, which shows that the matrix is deformed by the tensile stress given by the interface when the W–Y_2O_3 interface is separated. The white box area (W_1) was used for analysis, as shown in Fig. 4(b). This

area includes the red box area W_{BCC} and the blue box area W_{FCC}. The high-resolution image of the red box area is Fig. 4(c), the illustration is the FFT pattern in the area, the d spacings of the two basic lattice vectors are d_1=0.2277 nm$(011)_{BCC}$ and d_2=0.1573 nm$(200)_{BCC}$, the basic lattice vector distance is 90°, which conforms to the orientation relationship of crystal ribbon axis $[01\bar{1}]_{BCC}$. The high-resolution image of the blue box closer to the strain area is Fig. 4(d), the spacings of the two basic lattice vectors in the FFT pattern are d_1=0.1461 nm$(220)_{FCC}$, and d_2=0.2417 nm$(11\bar{1})_{FCC}$. The basic lattice vector distance is 90°, which conforms to the orientation relationship of crystal ribbon axis$[112]_{FCC}$. According to the comparison of the two sets of diffraction spots, the phase transition process has noticeable lattice distortion, and the phase transition is the primary stress release method in the deformation process. The selected area of Fig. 4(e) is the location of the orange box in Fig. 4(b), and the parallelogram corresponding to the fast Fourier diagram is shown in the white box in the illustration, which is located between W_{bcc} and W_{FCC}. D spacings of the two basic lattice vectors are 0.1613 and 0.2315 nm, and the basic lattice vector distance is 86°. The structure cannot be indexed to any area axis of W_{BCC} or W_{FCC}, and thus, it is regarded as an intermediate state. Given that the stress ends at this time and the FCC phase in the W matrix is unstable, this intermediate state is likely to be an instantaneous capture of the FCC→BCC phase transition process. The BCC→FCC phase transition caused by deformation can only occur in the environment around the interface and not in the main body of the matrix. The crystallographic mechanism transformation of BCC→FCC is considered to be the lattice shear in $[01\bar{1}]_{BCC}$, as shown in Fig. 4(f). According to the position of the middle

phase in Fig. 4(e), the crystal lattice is distorted clockwise, and finally, the phase change of BCC→FCC is completed. The lattice correspondence between the two phases is defined as$(01\bar{1})_{BCC}//(112)_{FCC}$ and $(011)_{BCC}//(2\bar{2}0)_{FCC}$, and this phase transition process corresponds to the Pitsch model[31]. After phase transition, $(11\bar{1})_{FCC}$ surface (d2=0.2417 nm) in $[112]_{FCC}$ corresponds to the diffraction spot value (d_1=0.2386 nm, d_2=0.2392 nm) of the torn W in Fig. 3(f), which further proves that the torn W is in FCC phase, and the torn part is the phase transited part of W_1. Certain stress exists on the Y_2O_3–W interface during the high-temperature tensile fracture process. Unlike previous W–Y_2O_3 semi-coherent interface that broke directly at room temperature[32], phase transition at the interface at high temperature is an effective way to relieve stress. The bonding force at W–Y_2O_3 interface can lead to BCC→FCC phase transition of W matrix, which provides strong support for tearing off the FCC phase W matrix at the Y_2O_3 interface.

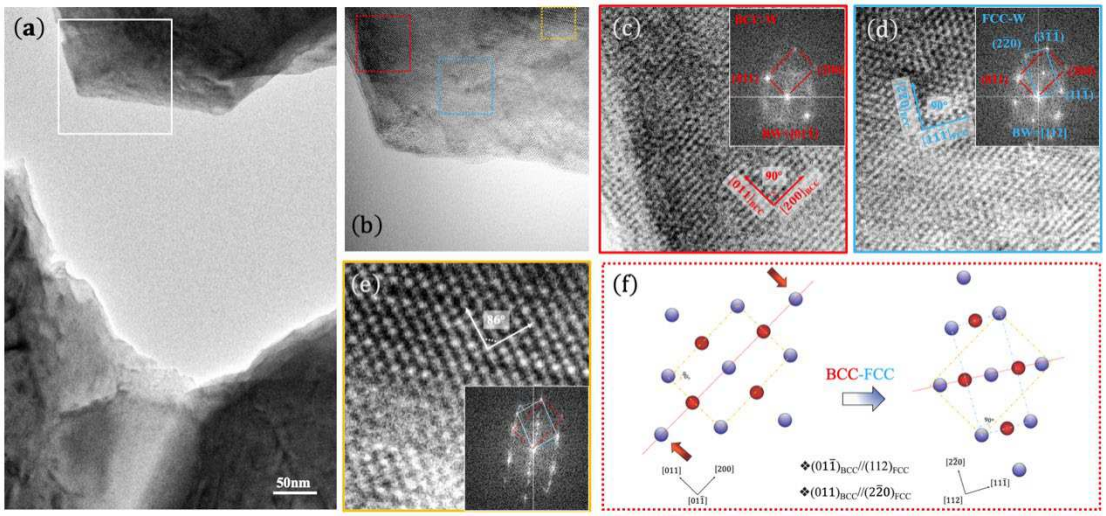

Fig. 4. HRTEM observation of BCC–FCC phase transition near the interface under tensile load at 1273 K (a) TEM bright-field image of the sample after tensile fracture of W–Y_2O_3 at 1273 K, (b) HRTEM after fracture of W_1 and Y_2, (c) HRTEM of the red frame in Fig. b, the illustration shows the FFT pattern in the red frame, (d) HRTEM of the blue frame in Fig. b, the illustration shows the FFT pattern in the blue

frame, (e) HRTEM of the orange frame in Fig. b, the illustration shows the FFT pattern in the orange frame, (f) crystallographic diagram of BCC–FCC phase transition

MD stretching simulation at room temperature and 1273 K: We used MD to simulate the tensile phase transition process of the W_1 matrix to determine further the effect of temperature on the phase transition process. As shown in Fig. 5(a), the model sample contains approximately 108000 tungsten atoms, and the coordinates are x axis[211], y axis[$01\bar{1}$], and z[$\bar{1}11$]axis. Tension was applied along the x-axis [211] at a constant strain rate until it was broken. The model corresponds to $[01\bar{1}]_{BCC}$ in Fig. 4(c). Common neighbor analysis command was used in Open Visualization Tool (OVITO), where the balls represent the W atoms in the BCC phase, green balls indicate the W atoms in the FCC phase, red and white indicate W atoms in the HCP phase, and other structures. The model was stretched after applying room temperature (293 K) and 1273 K. The model profile and overall FCC phase atom diagram are shown in Figs. 5(b–c). At room temperature, only a tiny amount of FCC phase atoms are generated at room temperature when the strain rate reaches 12% (Fig. 5b). When the strain rate goes 14%, FCC phase atoms disappear, indicating nearly no phase transition at room temperature. Studies have shown that plastic deformation under the temperature of BCC metal DBTT depends on the proliferation and cross-slip of dislocations; the mobility of screw dislocations also increases with temperature, which makes BCC metal plasticity strongly dependent on temperature[33]. At 1273 K, the strain rate of 12% causes many W atoms in the FCC phase, which accounts for 1.6% of the total atoms. As the strain rate reaches 14%, the number of W atoms in the FCC phase reaches a

peak, and it accounts for nearly 2.8% of the total, which shows a clear contrast with the stretching at room temperature. Compared with the MD analysis[27] of W single-crystal stretching at other orientations, the temperature is an essential factor that affects whether the phase transition occurs in the plastic deformation process of W. Fig. 5(d) is the enlarged view of the red circle in Fig. 5(c). According to the position of the coordinate axis of the atoms, part of $[01\bar{1}]_{BCC}$ structure is transited to $[112]_{FCC}$ structure, which causes lattice correspondence in $(01\bar{1})_{BCC}//(112)_{FCC}$. The process conforms to the Pitsch[31] model and fully corresponds to the W_1 phase transition at $W–Y_2O_3$ interface in Fig. 4. The crystallographic transition mechanism corresponding to this process is shown in Fig. 4(e). The phase transition process is expressed as

$$[01\bar{1}]_{BCC} \xrightarrow{\text{Pitsch}} [112]_{FCC}$$

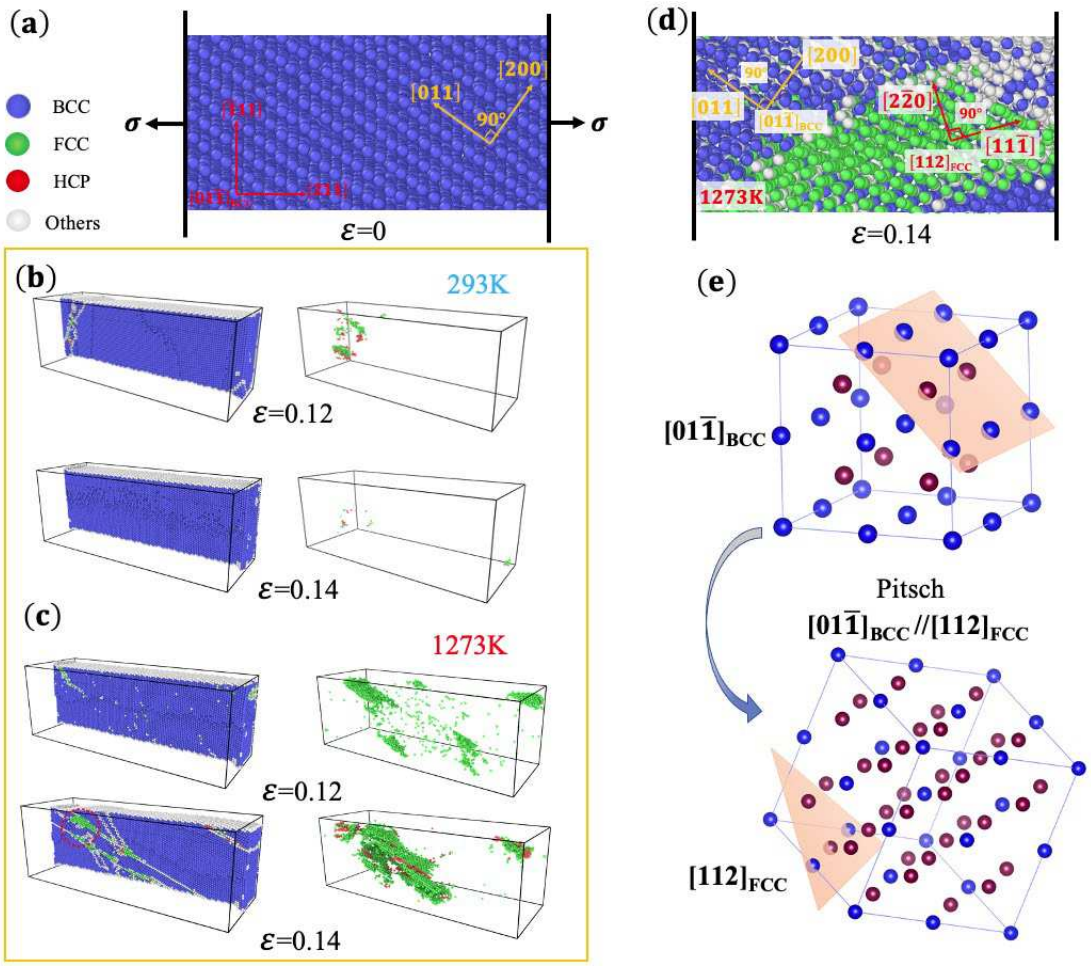

Fig. 5. MD stretching simulation at room temperature and 1273 K (a) W single-crystal stretching along [211] at the initial state, (b–c) screenshot when the strain rates are 12% and 14% at room temperature and 1273 K, (d) partially enlarged view at the red dotted frame in Fig. c, (e) crystallographic mechanism of the MD phase transition process, and corresponding Pitsch phase transition process

First-principle calculation of interface energy of ODS-W alloy phases: The abovementioned experimental phenomena all point to an important piece of information. The comparison of the interface bonding strength between Y_2O_3 and W with different crystal structures can predict the preferential breakage position, from which the experimental phenomenon can be reasonably explained. The ideal work of adhesion (W_{ad}) was used to describe the interface bonding strength[34-36]. This parameter

refers to the reversible work required to separate the interface into two free surfaces while ignoring the plasticity and diffusion degrees of freedom. It depends on the type of interface atoms and the electronic structure. The adhesion work W_{ad}, as one of the key parameters describing the bonding strength of interface atoms, can be used to measure the stability of the interface. The calculation formula of W_{ad} is as follows:

$$W_{ad} = (E_A^{slab} + E_B^{slab} - E_{AB}^{total})/S \quad (1)$$

where W_{ad} is the interface adhesion work; E_A^{slab}, E_B^{slab}, and E_{AB}^{total} refers to the total energy of surfaces A, B, and A/B interface system, respectively; S is the interface area.

According to experimental results of in situ stretching TEM, the W matrix at the interface undergoes a phase transition from BCC to FCC, and the FCC phase W matrix is torn off by Y_2O_3. On this basis, the W_{ad} of Y_2O_3/FCC-W interface, Y_2O_3/BCC-W interface, and BCC-W/FCC-W interface, as well as that the interface in BCC-W matrix, were explored to elaborate the abovementioned experimental results. Fig. 6(a) shows the isolated $Y_2O_3(020)$ and FCC-W$(2\bar{2}0)$ surface, and the corresponding optimized $Y_2O_3(020)$/FCC-W$(2\bar{2}0)$ interface structure is shown in Fig. 6(b). At the interface, W binds well to O atoms on Y_2O_3 surface, with the bond length in the range of 1.85–2.05 Å and the interfacial distance of 1.801 Å. The corresponding work of adhesion W_{ad} is 0.368 eV/Å^2(Fig. 6b). Fig. 6(c) shows the isolated $Y_2O_3(020)$ and BCC-W(200) surface, and Fig. 6(d) shows the corresponding $Y_2O_3(020)$/BCC-W(200) interface with lower W_{ad} of 0.208 eV/Å^2. The longer bond length of 1.95–2.25 Å is consistent with the lower W_{ad}. As observed, different interface atomic arrangements between FCC-W$(2\bar{2}0)$ and BCC-W(200) cause different relative atoms positions when forming interface with

Y_2O_3(020). Thus, the bonding strength of W–O differs, and the interface energy is different eventually. In situ experiment proves that BCC-W/FCC-W interface exists in the form of BCC-W(211)/FCC-W($3\bar{1}\bar{1}$)interface. Notably, in the process of structural optimization of the interface, FCC-W tends to transit to BCC-W, which is consistent with the phenomenon observed by Dr. Zhang Jianfei[26] and further proves that FCC phase is unstable. Herein, UBER curve (universal binding energy relation) was adopted to estimate the adhesion work as shown in Supplementary Fig. 2. Instead of structure optimization, the electronic energy of fixed BCC-W/FCC-W interface structure with the interface spacing in the range of 1.70 ~ 3.10 Å was calculated. The maximum interface adhesion work in this interval is taken, and the corresponding spacing of this point is the best interface spacing. According to the curve, the optimal interface spacing of 1.90 Å corresponds to the maximum interface adhesion work of 0.243 eVÅ^2 (Fig. 6f). For the W_{BCC} matrix, its internal crystal plane has ultra-high adhesion energy (0.577 eV/Å^2, Fig. 6h). So far, we have obtained the inequality of interface bonding strength as follows:

$$W_{BCC}–W_{BCC} > W_{FCC}–Y_2O_3 > W_{BCC}–W_{FCC} > W_{BCC}–Y_2O_3 \qquad (2)$$

Accordingly, the ultra-high adhesion energy of W_{BCC} matrix indicates that tearing it off is nearly impossible, but the phase transition becomes an effective way to release the stress of the W matrix at high temperature. After the phase transition, the interface bonding strength of W_{BCC}–W_{FCC} is significantly lower than that of W_{BCC}–W_{BCC}, and even lower than that of W_{FCC} and Y_2O_3 interface. Therefore, the fracture occurs at the W_{BCC}–W_{FCC} interface, which enables the Y_2O_3 interface to tear off the W_{FCC} matrix.

This condition explains why all the torn W exhibits FCC phase. Given that W_{BCC}–Y_2O_3 shows the lowest interface bonding strength, if no phase transformation occurs, then the pure W_{BCC} would not be torn off by Y_2O_3 and the fracture would occur at the W_{BCC}–Y_2O_3 interface. At room temperature, none phase transition occurs to promote tearing phenomenon. The crack will extend all the way to the matrix along Y_2O_3. Therefore, W–Y_2O_3 alloy only shows ordinary second phase strengthening effect at room temperature, but the strengthening effect of second-phase transformation at high temperature is reflected.

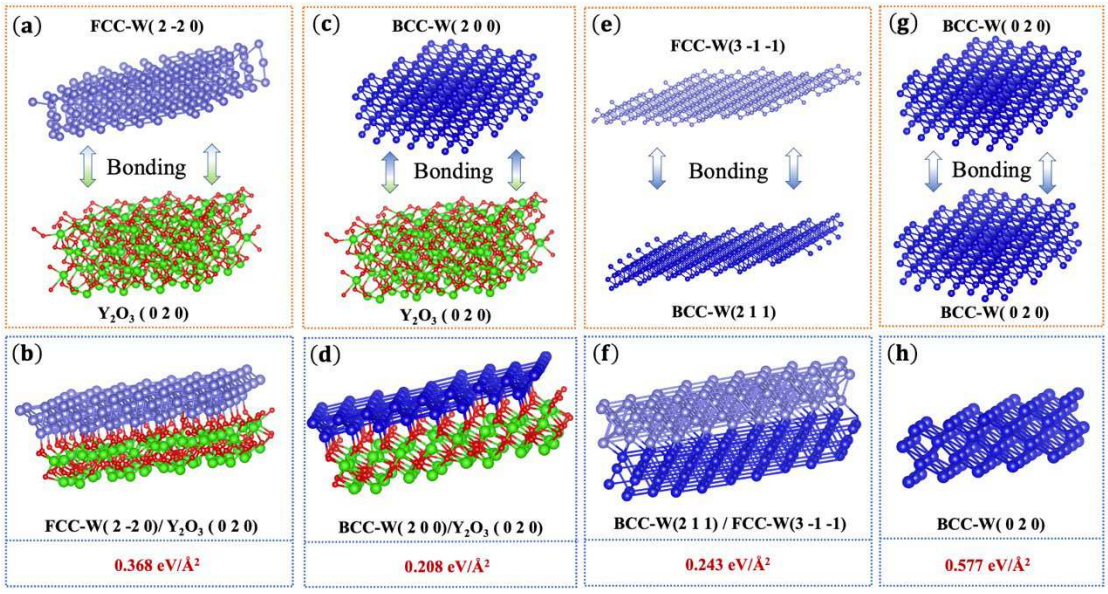

Fig. 6. First-principle simulation of interface energy of W–Y_2O_3 alloy phases (a) FCC-W($2\bar{2}0$)/Y_2O_3(020) bonding, (b) work of adhesion at W_{FCC}–Y_2O_3 interface, (c) BCC-W(200)/Y_2O_3(020) bonding, (d) work of adhesion at W_{BCC}–Y_2O_3 interface, (e) BCC-W(211)/FCC-W($3\bar{1}\bar{1}$) bonding, (f) work of adhesion at W_{BCC}–W_{FCC} interface, (g) BCC-W(200)/BCC-W(200) bonding, (h) work of adhesion at W_{BCC}–W_{BCC} interface

In summary, HRTEM analysis during in situ high-temperature stretching shows that W transformed from BCC phase to FCC phase has higher activity. Combining MD

simulation and first-principle calculations confirms that W in the FCC phase has a stronger interfacial bonding force with the rare-earth oxide interface. In the stretching process, the crack preferentially selects the phase transition area. Thus, W in the FCC phase is separated from the matrix and sticks to the rare-earth oxide interface, similar to a water drop. This process helps absorb deformation energy and reduce local stress concentration, which prevents crack propagation and causes a ductile fracture. These observations supplement the new second-phase strengthening mechanism, fill the gap in the second-phase strengthening mechanism at high temperatures, and provide a new idea for strengthening BCC structural metals used at high temperatures.

Methods

Preparation of W–Y_2O_3 alloy block： W–Y_2O_3 alloy was prepared by wet chemical method combined with SPS. W–Y_2O_3 alloy precursor powder was obtained by combining W source [$(NH_4)_6H_2W_{12}O_{40}\cdot xH_2O$)] and Yttrium source [$(Y(NO_3)_3\cdot 6H_2O)$] and mixed in deionized water solution, and oxalic acid ($C_2H_2O_4\cdot 2H_2O$) and dispersant triethanolamine ($C_6H_{15}NO_3$) were added after stirring, which obtained W–Y_2O_3 precursor. The obtained precursor was placed in a tube furnace and reduced in a hydrogen atmosphere to obtain WY_2O_3 composite powder. W–Y_2O_3 alloy block with a density of 99% was finally obtained by SPS sintering.

MD calculation method: MD simulations were conducted by adopting the classical open-source code large-scale atomic/molecular massively parallel simulator[37]. The simulated single-crystal W nanowire was modeled as a cuboid with dimensions of 28.49

nm × 94.95 nm × 94.95 nm, where coordinate axes of X, Y, and Z were along the crystal orientations of $[211]$, $[01\bar{1}]$, and $[\bar{1}11]$, respectively. The sample contained a total of 108000 atoms. The interaction between W atoms was described by the Finnis–Sinclair-type potential proposed by Ackland and Thetford[38], the single-crystal W nanowire was uniaxially stretched along the X direction at a constant strain rate of 108 s^{-1} until failure. Periodic boundary condition was applied along the tensile direction of the nanowire, and the side surfaces were under the traction-free boundary conditions. During tensile deformation, the temperature was kept constant and the time step was taken as 1 fs. The simulations were performed at 1273 and 293 K for comparison. The atoms were colored according to their local crystal structure by using the common neighbor analysis method[39], and the dislocations were extracted based on the dislocation extraction algorithm[40]. Snapshot visualization was conducted using the OVITO software[41].

First-principle calculation method: The density functional theory calculations were performed with the Vienna Ab initio Simulation Package (VASP 5.4) based on projector augmented wave method[42-43]. Perdew–Burke–Ernzerhof functional within generalized gradient approximation was adopted to treat electronic exchange–correlation energy[44]. For W and Y_2O_3 surfaces, integration in Brillouin zone was performed to optimize geometric configuration using the k-point mesh of 1×1×1 on the basis of the Monkhorst–Pack scheme[45]. The plane-wave cutoff energy was set to 400 eV. The convergence criteria for structural optimization were set as 0.1E-04 eV and 0.03 eV/A for energy and force, respectively. The vacuum layer of 20 Å was used to

avoid interaction between adjacent layers.

References

1. Clouet E, Lae L, Epicier T, Lefebvre W, Nastar M, Deschamps A. Complex precipitation pathways in multicomponent alloys. *Nat. Mater* **5**, 482-488 (2006).
2. Curtin WA, Olmsted DL, Hector LG, Jr. A predictive mechanism for dynamic strain ageing in aluminium-magnesium alloys. *Nat. Mater* **5**, 875-880 (2006).
3. Coury FG, Kaufman M, Clarke AJ. Solid-solution strengthening in refractory high entropy alloys. *Acta Mater* **175**, 66-81 (2019).
4. Matsukawa Y, et al. The effect of crystallographic mismatch on the obstacle strength of second phase precipitate particles in dispersion strengthening: bcc Nb particles and nanometric Nb clusters embedded in hcp Zr. *Acta Mater* **102**, 323-332 (2016).
5. Gong J, Wilkinson AJ. A microcantilever investigation of size effect, solid-solution strengthening and second-phase strengthening for a prism slip in alpha-Ti. *Acta Mater* **59**, 5970-5981 (2011).
6. Li D, et al. Enhanced strength in pure Ti via design of alternating coarse- and fine-grain layers. *Acta Mater* **206**, 116627 (2021).
7. Delince M, Jacques P, Pardoen T. Separation of size-dependent strengthening contributions in fine-grained Dual Phase steels by nanoindentation. *Acta Mater* **54**, 3395-3404 (2006).
8. Dong Z, Ma Z, Liu Y. Accelerated sintering of high-performance oxide dispersion strengthened alloy at low temperature. *Acta Mater* **220**,117309 (2021).
9. Li Z, Pradeep KG, Deng Y, Raabe D, Tasan CC. Metastable high-entropy dual-phase alloys overcome the strength-ductility trade-off. *Nature* **534**, 227-230 (2016).
10. Yang Y, et al. Bifunctional nanoprecipitates strengthen and ductilize a medium-entropy alloy. *Nature* **595**, 245-249 (2021).
11. Wang M, Huang MX. Abnormal TRIP effect on the work hardening behavior of a quenching and partitioning steel at high strain rate. *Acta Mater* **188**, 551-559 (2020).
12. Nogami S, Hasegawa A, Fukuda M, Rieth M, Reiser J, Pintsuk G. Mechanical properties of tungsten: Recent research on modified tungsten materials in Japan. *J. Nucl. Mater* **543**, 152506 (2021).
13. Luo LM, Zhao ZH, Yao G, Wu YC. Recent progress on preparation routes and

performance evaluation of ODS/CDS-W alloys for plasma facing materials in fusion devices. *J. Nucl. Mater* **548**,152857 (2021).

14. Chen H, et al. Effect of surface quality on hydrogen/helium irradiation behavior in tungsten. *Nucl Eng Technol*, (2021).doi: https://doi.org/10.1016/j.net.2021.12.006.

15. Hu W, Dong Z, Yu L, Ma Z, Liu Y. Synthesis of W-Y2O3 alloys by freeze-drying and subsequent low temperature sintering: Microstructure refinement and second phase particles regulation. *J. Mater Sci Technol* **36**, 84-90 (2020).

16. Yao G, et al. Isotropic thermal conductivity in rolled large-sized W-Y2O3 bulk material prepared by powder metallurgy route and rolling deformation technology. *Fusion Eng. Des* **137**, 325-330 (2018).

17. Salur E, Aslan A, Kuntoğlu M, Acarer M. Effect of ball milling time on the structural characteristics and mechanical properties of nano-sized Y2O3 particle reinforced aluminum matrix composites produced by powder metallurgy route. *Adv Powder Technol* **32**, 3826-3844 (2021).

18. Dong Z, Ma Z, Yu L, Liu Y. Achieving high strength and ductility in ODS-W alloy by employing oxide@W core-shell nanopowder as precursor. *Nat. Commun* **12**, 5052 (2021).

19. Wang QN, Wang JW, Li JX, Zhang Z, Mao SX. Consecutive crystallographic reorientations and superplasticity in body-centered cubic niobium nanowires. *Sci. Adv* **4**, eaas8850 (2018).

20. Wang SJ, Wang H, Du K, Zhang W, Sui ML, Mao SX. Deformation-induced structural transition in body-centred cubic molybdenum. *Nat. Commun* **5**, 3433 (2014).

21. Hsiung LL. Shock-induced phase transformation in tantalum. *J Phys Condens Matter* **22**, 385702 (2010).

22. A.L. Ruoff, H. Xia, Q. Xia, *Rev. Sci. Instrum* **63,** 4342 (1992).

23. Wang J, Zeng Z, Weinberger CR, Zhang Z, Zhu T, Mao SX. In situ atomic-scale observation of twinning-dominated deformation in nanoscale body-centred cubic tungsten. *Nat. Mater* **14**, 594-600 (2015).

24. Wang X, Wang J, He Y, Wang C, Zhong L, Mao SX. Unstable twin in body-centered cubic tungsten nanocrystals. *Nat Commun* **11**, 2497 (2020).

25. Wang JW, et al. Anti-twinning in nanoscale tungsten. *Sci. Adv* 6,essy2792 (2020).

26. Zhang J, et al. Timely and atomic-resolved high-temperature mechanical investigation of ductile fracture and atomistic mechanisms of tungsten. *Nat. Commun* **12**, 2218 (2021).

27. Ma B, Rao Q, He Y. Molecular dynamics simulation of temperature effect on tensile mechanical properties of single crystal tungsten nanowire. *Comput. Mater. Sci* **117**, 40-44 (2016).

28. Han X, et al. Double-tilt sample holder for transmission electron microscope.). Google Patents (2018).

29. Han, X. et al. Double-tilt In-situ Mechanical Sample Holder for Tem Based on Piezoelectric Ceramic Drive. U. S. Patent Application US10103001B2 (2018).

30. Chopra KL, Randlett MR, Duff RH. Face-Centered-Cubic Tungsten Films Obtained By. *Appl. Phys. Lett* **9**, 402-405 (1966).

31. Pitsch W. The martensite transformation in thin foils of iron-nitrogen alloys. *Philos Mag* **4**, 577-584 (1959).

32. Yao G, et al. Excellent performance of W–Y2O3 composite via powder process improvement and Y2O3 refinement. *Mater Design* **212**,110249 (2021).

33. Lu Y, Zhang YH, Ma E, Han WZ. Relative mobility of screw versus edge dislocations controls the ductile-to-brittle transition in metals. *Proc Natl Acad Sci USA* **118 (37),** e2110596118 (2021).

34. Siegel Donald J, Louis G. Hector Jr and James B. Adams. "First-principles study of metal–carbide/nitride adhesion: Al/VC vs. Al/VN." *Acta Mater* **50(3)**, 619-631 (2002).

35. Xiong H, Cao C, Chen G, Liu B. Revealing the adhesion strength and electronic properties of Ti3SiC2/Cu interface in Ti3SiC2 reinforced Cu-based composite by a first-principles study. *Surf. Interfaces* **27**, 101467 (2021).

36. Zhang K, Zhan Y. Adhesion strength and stability of Cu(111)/TiC(111) interface in composite coatings by first principles study. *Vacuum* **165**, 215-222 (2019).

37. Plimpton S. Fast parallel algorithms for short-range molecular dynamics. *J. Comput. Phys* **117**, 1-19 (1995).

38. Ackland GJ, Thetford R. An improvedN-body semi-empirical model for body-centred cubic transition metals. *Philos Mag A* **56**, 15-30 (1987).

39. Faken D, Jónsson H. Systematic analysis of local atomic structure combined with 3D computer graphics. *Comput. Mater. Sci* **2**, 279-286 (1994).

40. Stukowski A, Albe K. Extracting dislocations and non-dislocation crystal defects from atomistic simulation data. *Modelling Simul. Mater. Sci. Eng* **18**, 085001 (2010).

41. Stukowski A. Visualization and analysis of atomistic simulation data with OVITO–the Open Visualization Tool. *Modelling Simul. Mater. Sci. Eng* **18**,

015012 (2010).

42. Kresse G, Furthmiiller J. Efficiency of ab-initio total energy calculations for metals andsemiconductors using a plane-wave basis set. *Comput. Mater. Sci* **6**, 15-50 (1996).

43. Kresse G. Efficient iterative schemes for ab initio total-energy calculations using a plane-wave basis set. *Phys. Rev. B* **54**, 11169-11186 (1996).

44. Perdew JP, Burke K, Ernzerhof M. Generalized gradient approximation made simple. *Phys. Rev. Lett* **77**, 3865-3868 (1996).

45. Monkhorst HJ, Pack JD. Special points for Brillouin-zone integrations. *Phys. Rev. B* **13**, 5188-5192 (1976).

Acknowledgements

We acknowledge the funding support from the National Key Research and Development Program of China (2019YFE03120002), Natural Science Foundation of Anhui Province(2108085J21)**,** National Key Research and Development Program of Anhui Province(202104a05020045), and the 111 Project “New Materials and Technology for Clean Energy” (B18018).

Author Contributions

G.Q.W., L.M.L. and Y.C.W. conceived the project. G.Q.W., Q.Z., X.P.L. and Y.F.Z. planned and performed the experiments and collected and analyzed the data. H.X.L., Z.P.L. assisted with the experiments and characterizations. G.Q.W., L.M.L., X.P.L., Q.Z. and Y.C.W. co-wrote the manuscript. All authors discussed the results and commented on the manuscript.

Ethics declarations

Competing interests

The authors declare no competing interests.

Supplementary Files

This is a list of supplementary files associated with this preprint. Click to download.

- FractionalCoordinatesofrelatedcompounds.docx
- video.mp4
- sporting.docx